IEEE Journal of Microwaves

Received 27 March 2021; revised 20 May 2021; accepted 26 May 2021. Date of publication 24 June 2021; date of current version 7 July 2021.

Digital Object Identifier 10.1109/JMW.2021.3084947

On the Complete Radiation Pattern of a Vertical Hertzian Dipole Above a Low-Loss Ground

KRZYSZTOF A. MICHALSKI [1] (Life Fellow, IEEE), AND JUAN R. MOSIG [2] (Life Fellow, IEEE)

(Invited Paper)

[1]Texas A&M University, College Station, TX 77843-3128 USA
[2]École Polytechnique Fédérale de Lausanne, CH-1015 Lausanne, Switzerland

CORRESPONDING AUTHOR: Krzysztof A. Michalski (e-mail: k-michalski@tamu.edu).

Dedicated to the memory of Professor Tapan K. Sarkar.

ABSTRACT The complete radiation field pattern of a vertical Hertzian dipole antenna on or above a lossless or low-loss dielectric half-space is studied using a rigorous Sommerfeld formalism. The reflected fields in the air above the interface and the subsurface fields transmitted into the dielectric are computed by numerical integration of the Sommerfeld integrals. Furthermore, to facilitate the physical interpretation of these results, a detailed asymptotic saddle-point integration method analysis is presented, which includes terms that vary in magnitude with the second power of the inverse distance from the dipole. It is shown that the second-order field constituents are dominant at the interface, where the first-order geometrical fields vanish. These second-order terms comprise an evanescent wave propagating along the interface in the upper half-space and a lateral wave, also known as the head wave, which propagates in the subsurface along the direction of the critical angle. The two waves only exist between two cones whose half-angles are equal to the critical angle, and their interference with the geometrical-optics fields determines the radiation pattern for elevation angles near the horizon. The far zone surface fields on either side of the interface comprise two second order waves that propagate along the interface, one with the phase velocity in the air, and the other with the phase velocity in the dielectric. Away from the interface, the leading field components vary with the first power of the inverse distance, which explains the sharp dip in the field pattern at the interface—a phenomenon known as the interface pattern extinction. Another distinctive phenomenon, observed in the subsurface field pattern, is the rippling that occurs in the angular range between the critical angle cone and the interface. The asymptotic analysis has shown that this pattern scalloping results from the interference of the lateral wave with the geometrical-optics spherical wave.

INDEX TERMS Dipole antennas, antenna radiation patterns, interface pattern extinction, dielectric half-space, Sommerfeld integrals, saddle-point integration method, lateral waves.

I. INTRODUCTION

The problem of a vertical electric dipole (VED) radiating over a material half-space is fundamental to the understanding of antennas and wave propagation over ground. The first rigorous formulation of this problem was obtained by Sommerfeld [1], who expressed it in terms of the eponymous integrals. In view of the fact that this problem is not amenable to a closed form analytical solution, Sommerfeld and his followers resorted to various approximate procedures, usually assuming a high-loss ground [2]–[6]. Since the field propagating over ground was of primary interest, the field transmitted into the lower half-space received little attention, although there were some early exceptions [7]. Further studies of the transmitted field were spurred by the discovery of the so-called head wave in the acoustic half-space problem [8]. The corresponding electromagnetic problem was subsequently analyzed by the

recently-developed saddle-point integration method, and it was soon recognized that the head wave, later renamed lateral wave, was represented by a branch cut integral in the Sommerfeld formulation [9]–[11]. Nevertheless, this lateral wave, being a second-order effect with $\mathcal{O}(r^{-2})$ range dependence, was often ignored in subsequent studies, which only retained the leading first-order term with $\mathcal{O}(r^{-1})$ behavior [12]–[14]. The latter represents the geometric-optical field, which can also be obtained by the plane-wave reciprocity method [15]–[17]. The radiation field pattern of an interfacial VED over a low-loss half-space computed by this simple approach has a null at the interface and it exhibits subsurface peaking at the critical angle [13], [16], [18]. However, a rigorous analysis shows that the "interface pattern extinction" is not complete when the second-order effects are included. Furthermore, it is found that the rigorously computed subsurface pattern exhibits a scalloping for angles beyond the critical angle, which is absent in the geometric-optical pattern and is thus a second-order effect [16]. These second-order phenomena may be elucidated by the application of the saddle-point method, but the analysis is somewhat complicated by the fact that the standard procedure breaks down at the critical angle [19].

The understanding of subsurface radiation of antennas placed on or near an interface between two half-space media is fundamental in radio interferometry applications where the earth properties are those of a low-loss dielectric with moderate contrasts. A quantitative analysis of this problem is also of interest in wireless communications and sensing, where ever higher frequency bands are utilized and over a half of the radiated power may be transmitted into the ground as the losses become negligible. For example, for dry earth or urban ground we can assume the dielectric constant $\varepsilon_r' = 4$ and conductivity $\sigma = 10^{-4}$ S/m, which results in a loss tangent of 10^{-3} at 450 MHz.

In this paper, we present a study of the complete radiation pattern of a VED on or above a lossless or low-loss dielectric half-space, using the Sommerfeld formalism with the integrals evaluated numerically. Furthermore, to facilitate the physical interpretation of these results, we provide a detailed asymptotic saddle-point integration analysis, including effects of the second order in the inverse distance from the dipole. Our asymptotic procedure is not applicable at the critical angle, but this is not a major limitation, since the main objective of this work is to shed more light on the phenomena of interface pattern extinction and subsurface pattern scalloping observed in the angular range between the critical angle and the interface.

II. PROBLEM GEOMETRY AND NOTATION

Consider a z-oriented Hertzian dipole with the current moment $I\ell$ [Am], located on the z axis at a distance h above a dielectric half-space, as illustrated in Fig. 1. The free-space permeability, permittivity, intrinsic impedance, and wavenumber will be denoted by μ_0, ε_0, η_0 and k_0, respectively. The media are assumed non-magnetic and characterized relative to free space by the dielectric constants ε_n, $n = 1, 2$, with the corresponding wavenumbers $k_n = k_0\sqrt{\varepsilon_n}$ and intrinsic impedances $\eta_n = \eta_0/\sqrt{\varepsilon_n}$, and the media contrast will be specified by $\varepsilon = \varepsilon_2/\varepsilon_1$. The medium of the upper half-space will be assumed lossless, but the lower half-space may optionally have small lossless, in which case $\varepsilon_2 = \varepsilon_2' - j\varepsilon_2'' = \varepsilon_2'(1 - j\tan\delta_2)$, where $\tan\delta_2$ is the loss tangent of the lower medium. The $e^{j\omega t}$ time convention is assumed.

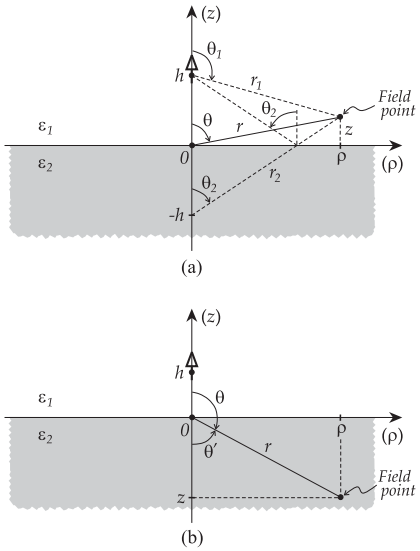

FIGURE. 1. Schematic of a vertical electric dipole located at a height *h* above a dielectric half-space when the field point is (a) above and (b) below the interface. Of interest is the radiation field pattern in both half-spaces at a constant radius *r*.

III. FORMULATION

The problem of Fig. 1 has cylindrical symmetry, with the electric and magnetic field components given as [20]

$$E_z = -j\omega\left(1 + \frac{1}{k_n^2}\frac{\partial^2}{\partial z^2}\right)A_z \tag{1}$$

$$E_\rho = -\frac{j\omega}{k_n^2}\frac{\partial^2 A_z}{\partial\rho\partial z}, \quad H_\varphi = -\frac{1}{\mu_0}\frac{\partial A_z}{\partial\rho} \tag{2}$$

where the subscript n corresponds to the half-space in which the field is evaluated, and where

$$A_z = \frac{\mu_0 I\ell}{2\pi\, j\omega\varepsilon_0\varepsilon_1}\int_0^\infty I_v^e(z|h)J_0(k_\rho\rho)k_\rho dk_\rho \tag{3}$$

is the z component of the magnetic vector potential, in which $J_0(\cdot)$ denotes the zero-order Bessel function and $I_v^e(z|h)$ is a Green function of the transmission-line network analogue of the layered medium, derived in Appendix A. We may express the vector potential in both half-spaces more explicitly as

$$A_{z1} = \frac{\mu_0 I\ell}{4\pi}k_1\left[\frac{e^{-j\Omega_1}}{\Omega_1} + \int_0^\infty \Gamma_\parallel \frac{e^{-jk_{z1}(z+h)}}{jk_{z1}}J_0(k_\rho\rho)\frac{k_\rho dk_\rho}{k_1}\right] \tag{4}$$

where $\Omega_1 = k_1 r_1$ and

$$A_{z2} = \frac{\mu_0 I\ell}{4\pi}k_1\int_0^\infty (1+\Gamma_\parallel)\frac{e^{-jk_{z1}h}}{jk_{z1}}e^{jk_{z2}z}J_0(k_\rho\rho)\frac{k_\rho dk_\rho}{k_1} \tag{5}$$

where we have introduced

$$\Gamma_{\parallel} \equiv -\overleftarrow{\Gamma}_1^e = \frac{k_{z1} - k_{z2}/\varepsilon}{k_{z1} + k_{z2}/\varepsilon}\,. \tag{6}$$

Note that A_{z1} in (4) comprises a direct, whole-space term and a "correction term" accounting for the lower half-space. The Sommerfeld integrals in (4) and (5) are over the transverse wavenumber k_ρ. Their integrands comprise the double-valued square-root functions k_{z1} and k_{z2} with branch points at $\pm k_1$ and $\pm k_2$, respectively, which necessitates the introduction of branch cuts in the $k_\rho-$plane, as discussed in Appendix B. It will be convenient for our purposes to employ the hyperbolic cuts illustrated in Fig. 16, and to introduce a four-sheeted Riemann surface defined in Fig. 17. The Sommerfeld integration path follows the positive-real axis on Sheet *I*, passing above the fourth-quadrant singularities, which in addition to the branch points k_1 and k_2 include a pole k_p. This Sommerfeld pole satisfies the dispersion relation $k_{z1} + k_{z2}/\varepsilon = 0$ obtained by equating to zero the denominator of the reflection coefficient (6).

The electromagnetic fields corresponding to the potentials A_{z1} and A_{z2} readily follow from (1)-(2). Assuming the normalization

$$\boldsymbol{E} = -j\eta_1 k_1^2 \frac{I\ell}{4\pi}\,\boldsymbol{\mathcal{E}}\,, \quad \boldsymbol{H} = -jk_1^2 \frac{I\ell}{4\pi}\,\boldsymbol{\mathcal{H}} \tag{7}$$

we find the electric field components in both half-spaces as

$$\mathcal{E}_{z1} = \mathcal{E}_{z1}^{\mathrm{D}} + \mathcal{E}_{z1}^{\mathrm{R}} \tag{8}$$

$$\mathcal{E}_{z1}^{\mathrm{D}} = \left[\sin^2\theta_1 - (1 - 3\cos^2\theta_1)\left(\frac{j}{\Omega_1} + \frac{1}{\Omega_1^2}\right)\right]\frac{e^{-j\Omega_1}}{\Omega_1} \tag{9}$$

$$\mathcal{E}_{z1}^{\mathrm{R}} = \int_0^\infty \Gamma_{\parallel}\,\frac{e^{-jk_{z1}(z+h)}}{jk_{z1}} J_0(k_\rho\rho)\,\frac{k_\rho^3 dk_\rho}{k_1^3} \tag{10}$$

$$\mathcal{E}_{z2} = \int_0^\infty \left(1 - \Gamma_{\parallel}\right)\,e^{-jk_{z1}h}\,\frac{e^{jk_{z2}z}}{jk_{z2}} J_0(k_\rho\rho)\,\frac{k_\rho^3 dk_\rho}{k_1^3} \tag{11}$$

$$\mathcal{E}_{\rho 1} = \mathcal{E}_{\rho 1}^{\mathrm{D}} + \mathcal{E}_{\rho 1}^{\mathrm{R}} \tag{12}$$

$$\mathcal{E}_{\rho 1}^{\mathrm{D}} = -\sin\theta_1\cos\theta_1\left[1 - 3\left(\frac{j}{\Omega_1} + \frac{1}{\Omega_1^2}\right)\right]\frac{e^{-j\Omega_1}}{\Omega_1} \tag{13}$$

$$\mathcal{E}_{\rho 1}^{\mathrm{R}} = \int_0^\infty \Gamma_{\parallel}\,e^{-jk_{z1}(z+h)} J_1(k_\rho\rho)\,\frac{k_\rho^2 dk_\rho}{k_1^3} \tag{14}$$

$$\mathcal{E}_{\rho 2} = \int_0^\infty -\left(1 - \Gamma_{\parallel}\right)\,e^{-jk_{z1}h} e^{jk_{z2}z} J_1(k_\rho\rho)\frac{k_\rho^2 dk_\rho}{k_1^3} \tag{15}$$

and the magnetic fields as

$$\mathcal{H}_{\varphi 1} = \mathcal{H}_{\varphi 1}^{\mathrm{D}} + \mathcal{H}_{\varphi 1}^{\mathrm{R}} \tag{16}$$

$$\mathcal{H}_{\varphi 1}^{\mathrm{D}} = -\sin\theta_1\left(1 - \frac{j}{\Omega_1}\right)\frac{e^{-j\Omega_1}}{\Omega_1} \tag{17}$$

$$\mathcal{H}_{\varphi 1}^{\mathrm{R}} = \int_0^\infty \Gamma_{\parallel}\,\frac{e^{-jk_{z1}(z+h)}}{k_{z1}} J_1(k_\rho\rho)\,\frac{k_\rho^2 dk_\rho}{k_1^2} \tag{18}$$

$$\mathcal{H}_{\varphi 2} = \int_0^\infty \left(1 + \Gamma_{\parallel}\right)\,\frac{e^{-jk_{z1}h}}{k_{z1}}\,e^{jk_{z2}z} J_1(k_\rho\rho)\,\frac{k_\rho^2 dk_\rho}{k_1^2}\,. \tag{19}$$

The radial component of the time-averaged Poynting vector is given as

$$S_r = \frac{1}{2}\,\Re e\, E_{\theta n} H_{\varphi n}^* = \eta_1 k_1^4 \frac{|I\ell|^2}{32\pi^2}\,\Re e\,\mathcal{E}_{\theta n}\mathcal{H}_{\varphi n}^* \tag{20}$$

where

$$\mathcal{E}_{\theta n} = -\sin\theta\,\mathcal{E}_{zn} + \cos\theta\,\mathcal{E}_{\rho n} \tag{21}$$

and the radiation pattern may be represented by the directive gain

$$\begin{aligned} D(r,\theta) &\equiv 4\pi\,\frac{r^2 S_r}{P_{\mathrm{rad}}} \\ &= \frac{3}{2}(k_1 r)^2\,\Re e\,\mathcal{E}_{\theta n}\mathcal{H}_{\varphi n}^* \approx \frac{3}{2}(k_1 r)^2\,|\mathcal{E}_{\theta n}|^2\sqrt{\frac{\varepsilon_n'}{\varepsilon_1}} \end{aligned} \tag{22}$$

where

$$P_{\mathrm{rad}} = \frac{|I\ell|^2}{12\pi}\eta_1 k_1^2 \tag{23}$$

is the power radiated by the dipole in an infinite homogeneous medium with the parameters of the upper half-space. It is understood in the above relations that $n = 1$ in the upper half-space ($\theta \le \pi/2$), and $n = 2$ in the lower half-space ($\theta \ge \pi/2$). Note that $P_{\mathrm{rad}}/(4\pi)$ may be interpreted as the power per unit solid angle radiated by an isotropic reference antenna. The radiation pattern of a VED has azimuthal symmetry, as there is no dependence on φ, and three Sommerfeld integrals need to be evaluated to compute $D(r,\theta)$ (or two integrals, if the approximation in (22) is employed). Since we wish to study the far-zone radiation pattern of the dipole, we will henceforth assume that $k_1 r \gg 1$ and focus on the transverse electric field components $\mathcal{E}_{\theta n}$.

IV. ASYMPTOTIC REFLECTED FIELD

Although the reflected field pattern of a VED on or above a material half-space is well understood [21], [22], we include here the saddle-point analysis of this problem for completeness. Furthermore, essentially the same method is employed in the next section in the analysis of the transmitted field pattern. It should be noted that there is no need to invoke the *modified* saddle-point method [23, Sec. 4.4a] here, in view of our assumption of lossless or low-loss lower half-space.

In the upper half-space of Fig. 1(*a*), we find $\mathcal{E}_{\theta 1} = \mathcal{E}_{\theta 1}^{D} + \mathcal{E}_{\theta 1}^{R}$, where

$$\begin{aligned} \mathcal{E}_{\theta 1}^{D} &= -\sin\theta\,\mathcal{E}_{z1}^{D} + \cos\theta\,\mathcal{E}_{\rho 1}^{D} \\ &\approx -\cos(\theta_1 - \theta)\sin\theta_1\,\frac{e^{-j\Omega_1}}{\Omega_1} \\ &\quad + j\left[\sin\theta + 3\sin(\theta_1 - \theta)\cos\theta_1\right]\frac{e^{-j\Omega_1}}{\Omega_1^2} \end{aligned} \tag{24}$$

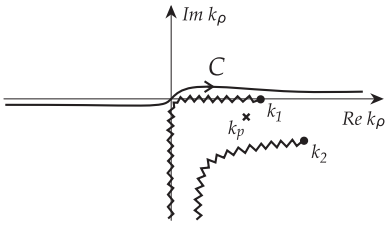

FIGURE. 2. Integration path *C* along the real axis on the top Riemann sheet.

and $\mathcal{E}^R_{\theta 1} = -\sin\theta\,\mathcal{E}^R_{z1} + \cos\theta\,\mathcal{E}^R_{\rho 1}$, where $\mathcal{E}^R_{z1}$ and $\mathcal{E}^R_{\rho 1}$ are given by (10) and (14), respectively. Note that in (24) we have retained terms up to the second order in Ω_1^{-1}. In order to evaluate the reflected field $\mathcal{E}^R_{\theta 1}$ asymptotically, we first express the Bessel functions in (10) and (14) in terms of the Hankel functions of the first and second kinds as $J_m(z) = \frac{1}{2}[H_m^{(1)}(z) + H_m^{(2)}(z)]$ and the extend the integration paths to the entire real axis via the formula $H_m^{(1)}(z\,e^{j\pi}) = -e^{-jm\pi}H_m^{(2)}(z)$, so that a typical Sommerfeld integral is transformed as

$$\int_0^\infty F(k_\rho)J_m(k_\rho\rho)k_\rho dk_\rho = \frac{1}{2}\int_{\infty e^{-j\pi}}^\infty F(k_\rho)H_m^{(2)}(k_\rho\rho)k_\rho dk_\rho \tag{25}$$

where $F(k_\rho)$ is an even function for $m = 0$ and odd for $m = 1$. The integration path in (25) runs just below a branch cut along the negative-real axis and a branch point at the origin, which are introduced by the Hankel function. However, this branch cut will not be encountered in the subsequent path transformations. To facilitate the application of the saddle-point method, we approximate the Hankel function by its large-argument form

$$H_m^{(2)}(k_\rho\rho) \sim \sqrt{\frac{2}{\pi k_\rho\rho}}\,e^{-j(k_\rho\rho - m\pi/2 - \pi/4)}\left(1 + j\,\frac{1-4m^2}{8k_\rho\rho}\right) \tag{26}$$

where we have retained the first two terms of the expansion. Since most of the contribution to the integrals arise from the vicinity of the saddle point, the use of this approximation will be justified as long as $k_1\rho \gg 1$. After these transformations, we obtain

$$\mathcal{E}^R_{z1} \approx \frac{1}{\sqrt{2j\pi}}\int_{\infty e^{-j\pi}}^\infty \Gamma_\parallel\,\frac{e^{-jk_{z1}(z+h)}}{k_{z1}}\,\frac{e^{-jk_\rho\rho}}{\sqrt{k_\rho\rho}} \times\left(1 + \frac{j}{8k_\rho\rho}\right)\frac{k_\rho^3 dk_\rho}{k_1^3} \tag{27}$$

and

$$\mathcal{E}^R_{\rho 1} \approx \frac{-1}{\sqrt{2j\pi}}\int_{\infty e^{-j\pi}}^\infty \Gamma_\parallel\,e^{-jk_{z1}(z+h)}\,\frac{e^{-jk_\rho\rho}}{\sqrt{k_\rho\rho}} \times\left(1 - \frac{3j}{8k_\rho\rho}\right)\frac{k_\rho^2 dk_\rho}{k_1^3} \tag{28}$$

where the integrals are along the real-axis path C on Sheet I of the $k_\rho-$plane, which is illustrated in Fig. 2. For simplicity, we have omitted in this figure the second-quadrant integrand singularities, as well as the branch cut along the negative-real axis contributed by the Hankel function, which will be inconsequential in the ensuing path deformations.

To facilitate the evaluation of the integrals in (27) and (28), we introduce a new variable of integration ξ via the transformation [23, Sec. 5.3c]

$$k_\rho = k_1\sin\xi \tag{29}$$

which implies $k_{z1} = k_1\cos\xi$ and $k_{z2} = k_1\kappa(\xi)$, where

$$\kappa(\xi) = \sqrt{\varepsilon - \sin^2\xi}\,. \tag{30}$$

We also convert to spherical coordinates via the substitutions $z + h = r_2\cos\theta_2$ and $\rho = r_2\sin\theta_2$, where r_2 is the radius of a field point in the upper half-space measured from the image dipole location and θ_2 is the specular angle of incidence, as indicated in Fig. 1(a). As a result of these steps, we obtain

$$\mathcal{E}^R_{\theta 1} \approx \frac{1}{\sqrt{\pi\Omega_2}}\int_C \Gamma_\parallel(\xi)f(\xi)\,e^{\Omega_2 q(\xi)}d\xi\,, \quad \Omega_2 = k_1 r_2 \tag{31}$$

where C is the ξ-plane image of the real-axis path on the top Riemann sheet of the k_ρ-plane, and where

$$q(\xi) = -j\cos(\xi - \theta_2) \tag{32}$$

$$\Gamma_\parallel(\xi) = \frac{\cos\xi - \kappa(\xi)/\varepsilon}{\cos\xi + \kappa(\xi)/\varepsilon} \tag{33}$$

and

$$f(\xi) = -\frac{\sin\xi}{\sqrt{2j}}\sqrt{\frac{\sin\xi}{\sin\theta_2}}\,\varpi(\xi) \tag{34}$$

with

$$\varpi(\xi) = \cos(\xi - \theta) + \frac{j}{8\Omega_2}\frac{\sin\theta}{\sin\theta_2}\,(1 - 3\cot\theta\cot\xi)\,. \tag{35}$$

The transformation (29) renders k_{z1} single valued and removes the associated branch cuts, so that sheets I and II of the Riemann surface of Fig. 17 in Appendix B are mapped into a single sheet of contiguous strips in the ξ-plane. The branch points $\pm k_1$ are mapped into regular points $\pm\pi/2$, but the branch points $\pm k_2$ and the branch cuts associated with k_{z2} persist in the new plane. We will refer to this sheet as the "top" or "proper" sheet, since it has the property that $\Im m\,k_{z2} < 0$ everywhere outside the branch cuts, on which $\Im m\,k_{z2} = 0$. Sheets III and IV are similarly transformed into the "bottom" or "improper" sheet on the ξ-plane, on which $\Im m\,k_{z2} > 0$ everywhere outside the branch cuts. The top sheet overlays the bottom sheet so that a continuous transition between these two sheets can only be effected by crossing one of the branch cuts. We illustrate the top sheet of the ξ-plane in Fig. 3 in the case where the medium of the lower half-space is slightly lossy. Since the transformation (29) is periodic along the real axis with a period of 2π, we only show one vertical stripe of width 2π centered at the origin, which is further subdivided into regions that correspond to the four quadrants of sheets I and II in the k_ρ-plane, with the sheets identified by Roman

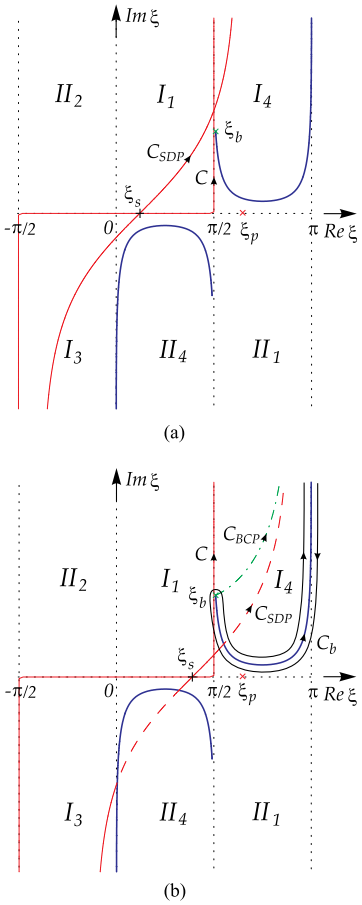

FIGURE. 3. Top Riemann sheet of the ξ-plane, which is a mapping of sheets *I* and *II* of the k_ρ-plane under the transformation $k_\rho = k_1 \sin\xi$. The Roman numerals indicate the mapped sheets and their subscripts indicate the quadrants, with the quadrant boundaries marked by dotted lines. On this sheet $\Im m\, k_{z2} < 0$ everywhere excepting the branch cuts, where $\Im m\, k_{z2} = 0$. Only the branch cuts involved in the subsequent path deformations are depicted and are drawn in solid blue lines, with the branch point ξ_b on sheet *I* indicated by the green cross symbol. The path *C*, which is the image of the real axis integration path in k_ρ−plane, is subsequently deformed into the steepest descent path C_{SDP} through the saddle point $\xi_s = \theta_2$, with both paths drawn in solid red lines. The top-sheet Sommerfeld pole ξ_p is indicated by the red cross symbol. To afford better picture clarity, a lossy case with $\varepsilon = 4 - j0.2$ is assumed. (a) $\theta_2 < \theta_{cb}$: C_{SDP} does not capture the branch point and approaches $j\infty$on the top sheet. (b) $\theta_2 > \theta_{cb}$: C_{SDP} captures the branch point and lies in part on the bottom sheet, as indicated by the dashed red line, which necessitates that the path wrapped around the branch cut C_b be added, so that $C_{SDP}$and the original path *C* may be reconnected on the top sheet at infinity. On the right side of C_b $\Re e\, k_{z2} > 0$, while on the left side $\Re e\, k_{z2} < 0$. The branch cut is subsequently deformed into the steepest descent path C_{BCP}, as shown by the dash-dot green line. The Sommerfeld pole is not captured by these path deformations.

numerals with subscripts indicating the quadrants. The path denoted by C is the mapping of the real-axis integration path on sheet I in Fig. 2 and the heavy lines show the mapping of the hyperbolic branch cuts associated with k_{z2} on sheets I and II. The branch point ξ_b, which corresponds to k_2 on sheet I in Fig. 2, and which plays an important role in the following analysis, satisfies the relations

$$\sin\xi_b = \sqrt{\varepsilon}\,, \quad \cos\xi_b = -j\sqrt{\varepsilon - 1} \tag{36}$$

from which we find

$$\xi_b = \xi_b' + j\xi_b'' = \pi/2 + j\log\left(\sqrt{\varepsilon} + \sqrt{\varepsilon - 1}\right) \tag{37}$$

and the Sommerfeld pole k_p is similarly mapped into

$$\xi_p = \frac{\pi}{2} + j\ln\left(\sqrt{\frac{\varepsilon}{\varepsilon+1}} - \frac{j}{\sqrt{\varepsilon+1}}\right). \tag{38}$$

To facilitate the evaluation of the integral in (31), we deform the path C into the steepest descent path (SDP) $C_{\rm SDP}$ passing through the saddle point ξ_s, where the latter may be found as a root of $q'(\xi) = 0$, where the prime indicates differentiation with respect of the argument of the function, and we readily show that $\xi_s = \theta_2$. The SDP is defined by the conditions $\Im m\, q(\xi) = \Im m\, q(\xi_s) =$ constant and $\Re e\, q(\xi) \le \Re e\, q(\xi_s)$, which in our case lead to

$$\cos(\xi' - \theta_2)\cosh\xi'' = 1 \tag{39}$$

where the notation $\xi = \xi' + j\xi''$ is implied, and we find that the SDP is given as

$$\xi' = \theta_2 \pm \operatorname{arccos\,sech}\,\xi''\,, \quad -\infty < \xi'' < \infty\,. \tag{40}$$

In this expression, the upper (lower) sign in should be selected in the positive (negative) range of ξ'', so that the SDP approaches the vertical asymptotes $\xi' = \theta_2 \pm \pi/2$. The integration along the SDP is most conveniently performed by introducing a new variable of integration s via the substitution $q(\xi) = q(\xi_s) - s^2$, which in our case becomes [24]

$$\cos(\xi - \theta_2) = 1 - js^2\,, \quad -\infty < s < \infty \tag{41}$$

with the Jacobian

$$\frac{d\xi}{ds} = \frac{\sqrt{2j}}{\sqrt{1 - js^2/2}} \underset{s\to 0}{\longrightarrow} \sqrt{2}\, e^{j\pi/4}\,. \tag{42}$$

It thus follows that the SDP in the ξ-plane passes through the saddle point θ_2 at an angle of $\pi/4$, as illustrated in Fig. 3. Upon solving (41) for ξ, we may express the SDP in terms of the real parameter s as [25]

$$\xi_{\rm SDP} = \theta_2 + j\ln\left[1 - js^2 + (1-j)s\sqrt{1 - js^2/2}\right]. \tag{43}$$

In the s-plane, the SDP is along the real axis, with the saddle point at the origin. The SDP contribution to $\mathcal{E}_{\theta 1}^R$ may now be found as

$$\mathcal{E}_{\theta 1}^{\rm SDP} \approx \frac{e^{-j\Omega_2}}{\sqrt{\pi\Omega_2}} \int_{-\infty}^{\infty} G(s)\, e^{-\Omega_2 s^2}\, ds \tag{44}$$

where

$$G(s) = \frac{d\xi}{ds}\, \Gamma_\parallel(\xi) f(\xi)\Big|_{\xi\,=\,\xi_{\rm SDP}}\,. \tag{45}$$

Referring to Fig. 3, we note that when the angle θ_2 exceeds a certain value, the SDP may cross the k_{z2} branch cut on II_4, enter the bottom sheet, and emerge again on the top sheet

when this branch cut is crossed for the second time. Furthermore, when θ_2 is further increased towards the interface, the SDP will eventually also cross the k_{z2} branch cut on I_4, which occurs for $\theta_2 > \theta_{cb}$, where θ_{cb} denotes the angle of capture of the branch point, which in view of (40) is given as

$$\theta_{cb} = \xi_b' - \operatorname{arccos}\operatorname{sech}\xi_b'' . \tag{46}$$

We can show that in the lossless case θ_{cb} is equal to the critical angle

$$\theta_c = \arcsin\left(1/\sqrt{\varepsilon}\right) \tag{47}$$

of a plane wave incident in the lower half-space. The integrand remains continuous along the SDP despite the branch cut crossings, which may be ensured by choosing the $\Re e\,\kappa > 0$ branch of the complex square root. Since the branch cut on I_4 is crossed only once when $\theta_2 > \theta_{cb}$, the SDP continues on the bottom sheet to $j\infty$, and in order to form a closed contour with the original path C on the top sheet of the ξ-plane, it is necessary to augment the SDP by a path around the branch cut C_b, as illustrated in Fig. 3(b). On this path $\Im m\,\kappa = 0$ with $\Re e\,\kappa > 0$ on the right side of the cut and $\Re e\,\kappa < 0$ on the left. The contribution to $\mathcal{E}_{\theta 1}^{R}$ from this branch cut path (BCP) is found as

$$\mathcal{E}_{\theta 1}^{\mathrm{BCP}} \approx \frac{1}{\sqrt{\pi\,\Omega_2}} \int_{C_b} [\![\Gamma_\parallel(\xi)]\!] f(\xi)\, e^{\Omega_2 q(\xi)} d\xi\,, \quad \theta_2 > \theta_{cb} \tag{48}$$

where

$$[\![\Gamma_\parallel(\xi)]\!] = \frac{4\cos\xi\,\kappa(\xi)/\varepsilon}{\cos^2\xi - \kappa^2(\xi)/\varepsilon^2}\,, \quad \Re e\,\kappa(\xi) > 0 \tag{49}$$

represents the jump in $\Gamma_\parallel(\xi)$ across the branch cut. It is advantageous for the convergence of the integral to deform C_b to the steepest descent path C_{BCP} emanating from the branch point ξ_b, which is permissible as there are no singularities in the region of the complex plane swept in this deformation. This new BCP may be determined as

$$\xi' = \theta_2 + \arccos\left[\cos(\xi_b' - \theta_2)\cosh\xi_b''\operatorname{sech}\xi''\right] \tag{50}$$

with $\xi_b'' \le \xi'' < \infty$, and we note that it approaches the vertical asymptote $\xi' = \theta_2 + \pi/2$ for $\xi'' \to \infty$. To evaluate (48) along C_{BCP} it will be convenient to introduce a new variable of integration s via the transformation $q(\xi) = q(\xi_b) - s^2$, which in our case becomes

$$\cos(\xi - \theta_2) = \cos(\xi_b - \theta_2) - js^2 \equiv \zeta(s)\,, \quad 0 \le s < \infty \tag{51}$$

with the Jacobian given as

$$\frac{d\xi}{ds} = \frac{2js}{\sqrt{1-\zeta^2(s)}} \tag{52}$$

and upon solving (51) for ξ we find

$$\xi_{\mathrm{BCP}} = \theta_2 + j\ln\left[\zeta(s) - j\sqrt{1-\zeta^2(s)}\right]. \tag{53}$$

Expressing the BCP integral in the s-plane we thus obtain

$$\mathcal{E}_{\theta 1}^{\mathrm{BCP}} \approx \frac{e^{-j\Omega_2\cos(\xi_b-\theta_2)}}{\sqrt{\pi\,\Omega_2}} \int_0^\infty B(s)\, e^{-\Omega_2 s^2} s\, ds\,, \quad \theta_2 > \theta_{cb} \tag{54}$$

where

$$B(s) = \frac{2j}{\sqrt{1-\zeta^2(s)}}\, [\![\Gamma_\parallel(\xi)]\!] f(\xi)\Big|_{\xi\,=\,\xi_{\mathrm{BCP}}}\,. \tag{55}$$

In view of the rapidly decreasing exponentials in the integrands of (44) and (54), the integrals may readily be evaluated by suitable numerical quadrature rules. However, to gain more insight into the behavior of the fields for $k_1 r \gg 1$, we will evaluate these integrals asymptotically by the saddle-point method with Ω_2 as the large parameter, retaining terms up to the second order in Ω_2^{-1}. We begin with $\mathcal{E}_{\theta 1}^{\mathrm{SDP}}$ and approximate $G(s)$ in (44) by the truncated Maclaurin series

$$G(s) \approx G(0) + G'(0)\, s + G''(0)\,\frac{s^2}{2} \tag{56}$$

where the primes indicate differentiation with respect to the function argument, and then integrate term-by-term in closed form [23, Sec. 4.2b], to obtain

$$\mathcal{E}_{\theta 1}^{\mathrm{SDP}} \approx \left[G(0) + \frac{G''(0)}{4\Omega_2}\right]\frac{e^{-j\Omega_2}}{\Omega_2}\,. \tag{57}$$

Note that it was necessary to retain the first three terms in (56) because the term odd in s integrates to zero. As a result, we obtain

$$\begin{aligned}\mathcal{E}_{\theta 1}^{\mathrm{SDP}} \approx {} & -\sin\theta_2\cos(\theta_2-\theta)\,\Gamma_\parallel(\theta_2)\frac{e^{-j\Omega_2}}{\Omega_2} \\ & -\sin\theta_2\,\frac{\Upsilon(\theta_2)}{8j}\,\frac{e^{-j\Omega_2}}{\Omega_2^2}\end{aligned} \tag{58}$$

where

$$\begin{aligned}\Upsilon(\theta_2) = {} & \left[\left(9 - 3\cot^2\theta_2\right)\cos(\theta_2-\theta)\right. \\ & \left. +12\cot\theta_2\sin(\theta_2-\theta) - (1 - 3\cot\theta_2\cot\theta)\right]\,\Gamma_\parallel(\theta_2) \\ & -\left[12\cos\theta_2\cos(\theta_2-\theta) - 8\sin(\theta_2-\theta)\right]\,\Gamma_\parallel'(\theta_2) \\ & -4\cos(\theta_2-\theta)\,\Gamma_\parallel''(\theta_2)\end{aligned} \tag{59}$$

with the required derivatives of the reflection coefficient listed in Appendix C. The leading first-order term in (58) represents the geometric-optical reflected field and the second-order term represents the diffraction field.

To derive the asymptotic form of $\mathcal{E}_{\theta 1}^{\mathrm{BCP}}$, we first approximate $B(s)$ in (54) by the two-term Maclaurin expansion

$$B(s) \approx B(0) + B'(0)s \tag{60}$$

in which $B(0) = 0$, since $s = 0$ corresponds to $\xi = \xi_b$ and $[\![\Gamma_\parallel(\xi_b)]\!] = 0$, and the coefficient $B'(0)$ may be found as

$$B'(0) = \lim_{s\to 0}\frac{B(s)}{s} = -\frac{4\sqrt{2j}}{\varepsilon}\sqrt{\frac{\sin\xi_b}{\sin\theta_2}}\tan\xi_b\,\frac{\cos(\xi_b-\theta)}{\sin(\xi_b-\theta_2)}\,\Lambda \tag{61}$$

where

$$\Lambda = \lim_{s\to 0} \frac{\kappa(\xi)}{s} \overset{\text{H}}{=} \sqrt{\frac{-2j\sin\xi_b\cos\xi_b}{\sin(\xi_b-\theta_2)}}\,. \tag{62}$$

After this substitution, the integral may be evaluated in a closed form, and we obtain

$$\mathcal{E}_{\theta 1}^{\text{BCP}} \approx \frac{B'(0)}{4\Omega_2^2}\, e^{-k_1\sqrt{\varepsilon-1}\,(z+h)}\, e^{-jk_2\rho} \tag{63}$$

where we have used (36) in the exponent. The branch cut contribution is thus a second-order effect with $\mathcal{O}(\Omega_2^{-2})$ range dependence. Furthermore, it is an inhomogeneous surface wave that propagates along the interface with the phase velocity corresponding to the medium of the lower half-space and decreases exponentially in the direction normal to the interface. In the lossy case with a complex-valued k_2, this wave also decreases exponentially as it propagates away from the dipole.

The complete asymptotic electric field $\mathcal{E}_{\theta 1}$ may now be found as

$$\mathcal{E}_{\theta 1} \approx \mathcal{E}_{\theta 1}^{D} + \mathcal{E}_{\theta 1}^{\text{SDP}} + \mathcal{U}(\theta-\theta_{cb})\,\mathcal{E}_{\theta 1}^{\text{BCP}} \tag{64}$$

where $\mathcal{U}(\cdot)$ denotes the Heaviside unit step function. When the dipole and the field point are at the interface ($h=0, \theta=\pi/2$), this reduces to

$$\mathcal{E}_{\theta 1} \approx \frac{2j\varepsilon}{(\varepsilon-1)}\left[\varepsilon\,\frac{e^{-jk_1\rho}}{(k_1\rho)^2} - \frac{1}{\sqrt{\varepsilon}}\,\frac{e^{-jk_2\rho}}{(k_1\rho)^2}\right] \tag{65}$$

which behaves as $\mathcal{O}(\rho^{-2})$, as a result of a partial cancellation of the direct and SDP fields. We note that the asymptotic interface field comprises two waves, one propagating with the phase velocity of the upper half-space, and the other with the phase velocity of the lower half-space.

It should be noted here that the Sommerfeld pole ξ_p in Fig. 3 is never encountered by the SDP, even for $\theta_2=\pi/2$, in view of its location in the fast wave region of the $\xi-$plane [26, Sec. 19.5]. Nevertheless, it may still be necessary to take this pole into account if it lies close to the saddle point, which can only occur if the lower half-space is highly lossy. In this case, the so-called modified saddle-point procedure should be employed, which contributes an extra term known as the Norton surface wave [22]. On the other hand, the branch cut contribution is then negligible.

V. ASYMPTOTIC TRANSMITTED FIELD

We find the transmitted field in the lower half-space of Fig. 1(*b*) from $\mathcal{E}_{\theta 2} = -\sin\theta'\,\mathcal{E}_{z2} - \cos\theta'\,\mathcal{E}_{\rho 2}$, where $\mathcal{E}_{z2}$ and $\mathcal{E}_{\rho 2}$ are given by the integrals (11) and (15), respectively. We then extend the integration path to the entire real axis and replace the Hankel function by its two-term asymptotic form, as in the case of the reflected field. After these transformations, we change the variable of integration via

$$k_\rho = k_2\sin\xi \tag{66}$$

which implies $k_{z2} = k_2\cos\xi$ and $k_{z1} = k_1\kappa(\xi)$, where

$$\kappa(\xi) = \sqrt{1-\varepsilon\sin^2\xi}\,. \tag{67}$$

Under the transformation (66), the four-sheeted Riemann surface in k_ρ-plane, as described in Appendix B, is mapped into a two-sheeted Riemann surface in the angular spectrum ξ-plane, with the top sheet of the latter shown in Fig. 4, where relatively high lower half-space losses are assumed for illustration purposes only. The substitution (66) removes the branch cuts associated with k_{z2}, but not those associated with k_{z1} remain. The branch point ξ_b, which is the image of k_1 from the $k_\rho-$plane in Fig. 2, satisfies the relationships

$$\sin\xi_b = \frac{1}{\sqrt{\varepsilon}}\,, \quad \cos\xi_b = \sqrt{1-\frac{1}{\varepsilon}} \tag{68}$$

from which we find

$$\xi_b = -j\ln\left(\frac{j}{\sqrt{\varepsilon}} + \sqrt{1-\frac{1}{\varepsilon}}\right) \tag{69}$$

and the Sommerfeld pole k_p is similarly mapped into

$$\xi_p = -j\ln\left[\frac{j}{\sqrt{\varepsilon+1}} + \sqrt{\frac{\varepsilon}{\varepsilon+1}}\right]. \tag{70}$$

These transformations and the substitutions $z = -r\cos\theta'$ and $\rho = r\sin\theta'$, where θ' is the supplementary elevation angle indicated in Fig. 1(*b*), allow us to express $\mathcal{E}_{\theta 2}$ as

$$\mathcal{E}_{\theta 2} \approx \frac{1}{\sqrt{\pi\Omega}}\int_C F(\xi)\, e^{\Omega q(\xi)}\, d\xi\,, \quad \Omega = k_2 r \tag{71}$$

with

$$q(\xi) = -j\left[\cos(\xi-\theta') + \frac{h}{r}\,\frac{\kappa(\xi)}{\sqrt{\varepsilon}}\right] \tag{72}$$

$$F(\xi) = -\frac{g(\xi)}{\sqrt{2j}}\sqrt{\frac{\sin\xi}{\sin\theta'}}\,\varpi(\xi) \tag{73}$$

$$g(\xi) = \frac{2\varepsilon\,\cos\xi\sin\xi}{\kappa(\xi) + \dfrac{\cos\xi}{\sqrt{\varepsilon}}} \tag{74}$$

$$\varpi(\xi) = \cos(\xi-\theta') + \frac{j}{8\Omega}\left(1 - 3\cot\theta'\cot\xi\right). \tag{75}$$

The integration path C in (71), which is the image of the real-axis path in Fig. 2, is illustrated in Fig. 4. To efficiently evaluate the integral in (71), we deform C into the steepest-descent path C_{SDP} passing through the saddle point ξ_s, where the latter is a root of the equation

$$q'(\xi) = j\left[\sin(\xi-\theta') + \frac{h}{r}\sqrt{\varepsilon}\,\frac{\sin\xi\cos\xi}{\kappa(\xi)}\right] = 0\,. \tag{76}$$

We further introduce the transformation

$$q(\xi) = q(\xi_s) - s^2 \tag{77}$$

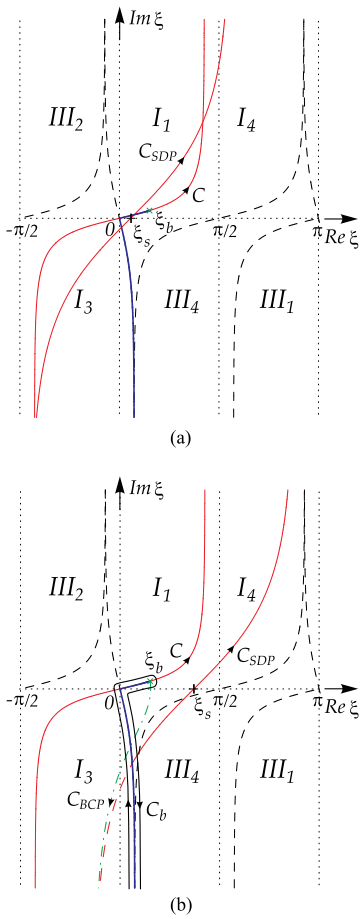

FIGURE. 4. **Top Riemann sheet of the ξ-plane, which is a mapping of sheets *I* and *III* of the k_ρ-plane under the transformation $k_\rho = k_2 \sin\xi$. The Roman numerals indicate the mapped sheets and their subscripts indicate the quadrants, with the quadrant boundaries marked by dashed black lines. On this sheet $\Im m\, k_{z1} < 0$ everywhere excepting the branch cuts, where $\Im m\, k_{z1} = 0$. Only the branch cut involved in the subsequent path deformations is depicted and is drawn in a solid blue line, with the branch point ξ_b indicated by a green cross symbol. The path *C*, drawn in a solid red line, is the image of the real axis integration path in k_ρ-plane. This path is subsequently deformed into the steepest descent path C_{SDP} through the saddle point $\xi_s = \theta'$. Not shown is the Sommerfeld pole ξ_p, which lies in I_4 very close to ξ_b just below the branch cut. To afford better picture clarity, the plots were generated for a lossy case with $\varepsilon = 4 - j2$.**
(*a*) $\theta' < \theta_{cb}$. C_{SDP} crosses the branch cut twice with the saddle point θ' located on the bottom sheet path segment between the crossings.
(*b*) $\theta' > \theta_{cb}$. C_{SDP} crosses the branch cut once and lies in part on the bottom sheet, as indicated by the dashed red line, which necessitates that the path wrapped around the branch cut C_b be added, so that C_{SDP} and the original path *C* may be reconnected on the top sheet at infinity. On the left side of C_b $\Re e\, k_{z1} > 0$, while on the right $\Re e\, k_{z1} < 0$. The branch cut is subsequently deformed into the steepest descent path C_{BCP}, as shown by the dash-dot green line. The Sommerfeld pole is not captured by these path deformations.

which maps the SDP into the real axis in the s-plane and the saddle point into the origin, and we may express (71) as

$$\mathcal{E}_{\theta 2}^{\mathrm{SDP}} \approx \frac{e^{\Omega q(\xi_s)}}{\sqrt{\pi\,\Omega}} \int_{-\infty}^{\infty} G(s)\, e^{-\Omega s^2}\, ds \tag{78}$$

with

$$G(s) = \frac{d\xi}{ds} F(\xi)\Big|_{\xi\,=\,\xi_{\mathrm{SDP}}} \tag{79}$$

which presumes that ξ_{SDP} is expressed in terms of s via (77). The Jacobian of the transformation is found as

$$\frac{d\xi}{ds} = \frac{-2s}{q'(\xi)} \underset{s\to 0}{\longrightarrow} \sqrt{\frac{-2}{q''(\xi_s)}} \tag{80}$$

where

$$q''(\xi) = j\left\{\cos(\xi - \theta') + \frac{h}{r}\sqrt{\varepsilon} \cdot \left[\frac{1 - 2\sin^2\xi}{\kappa(\xi)} + \varepsilon\,\frac{\sin^2\xi\cos^2\xi}{\kappa^3(\xi)}\right]\right\}. \tag{81}$$

For arbitrary values of $h/r > 0$, a closed form solution of (76) is not available and an explicit expression of the SDP in terms of s cannot be obtained. The saddle point can in this case be found by a numerical root search in the complex ξ-plane, or alternatively (76) can be converted to a quartic polynomial equation in $\sin^2\xi_s$, which yields four candidate roots on the top and bottom Riemann sheets. To avoid these complications, we will henceforth assume that $h/r \ll 1$ and separate the factor

$$\psi(\xi) = e^{-jk_1 h\kappa(\xi)} \tag{82}$$

from the exponential in (71) and include it in $F(\xi)$. This simplifies (72) to $q(\xi) = -j\cos(\xi - \theta')$ and the saddle point is found at $\xi_s = \theta'$, with $q(\xi_s) = -j$, hence the saddle-point method procedure of the previous section is applicable with θ' and Ω substituted for θ_2 and Ω_2, respectively. The ξ-plane is of course different, since the transformation (66) is now employed, but the SDP is still given by (43), except with θ' taking the place of θ_2, so that C_{SDP} now passes through the saddle point $\xi_s = \theta'$, as illustrated in Fig. 4. When $\theta' > 0$, C_{SDP} encounters the branch cut and it can either be deformed to bypass it while remaining entirely on the top sheet, or it can be allowed to cross the branch cut unperturbed and enter the bottom sheet, which is the preferred approach and we follow it here. For a sufficiently large θ' the SDP will capture the branch point, with the angle of capture θ_{cb} still given by (46), which in the lossless case is equal to the critical angle θ_c (47). Note that for $\theta' < \theta_{cb}$ the SDP crosses the branch cut twice and the saddle point $\xi_s = \theta'$ is located on the bottom sheet path segment extending between the two crossings, whereas for $\theta' > \theta_{cb}$ the SDP crosses the branch cut only once with the saddle point on the top sheet, as depicted in Fig. 4 (a) and (b), respectively. However, in the latter case the SDP originates on the bottom sheet and it must be augmented by the path C_b around the branch cut, so that the deformed path and the original path C may be reconnected at infinity on the top sheet [27, Sec. 15.8]. To effect a continuous transition between the sheets when the branch cut is crossed along the SDP, we should select the branch of κ with $\Re e\,\kappa > 0$ when $\theta' \le \theta_{cb}$, and the branch with $\Re e\,\kappa < 0$ when $\theta' > \theta_{cb}$. It

should be noted that the Sommereld pole ξ_p, which lies on the top sheet just below the branch cut and to the left of ξ_b in Fig. 4, is never encountered by the SDP as it sweeps through the bottom sheet region near the pole location for $\theta' < \theta_{cb}$.

We will now evaluate the integral in (78) asymptotically by the saddle-point method with $\Omega = k_2 r$ as the large parameter, retaining terms up to the second order in Ω^{-1}. Since we allow the possibility of small losses in the lower half-space, it will be convenient to first obtain an asymptotic expansion for real values of Ω and then continue Ω analytically into a range of complex values [23, p. 370]. We first approximate $G(s)$ by a truncated Maclaurin series, as in (56), and then integrate term-by-term in closed form to obtain

$$\begin{aligned}\mathcal{E}_{\theta 2}^{\mathrm{SDP}} \approx & -g(\theta')\,\psi(\theta')\,\frac{e^{-j\Omega}}{\Omega} \\ & + \frac{1}{2j}\left\{g''(\theta') + g'(\theta')\left[\cot\theta' + 2\frac{\psi'(\theta')}{\psi(\theta')}\right]\right. \\ & \left. - g(\theta')\left[\frac{1}{\sin^2\theta'} - \cot\theta'\frac{\psi'(\theta')}{\psi(\theta')} - \frac{\psi''(\theta')}{\psi(\theta')}\right]\right\}\psi(\theta')\,\frac{e^{-j\Omega}}{\Omega^2}\end{aligned} \tag{83}$$

where the required derivatives of $g(\xi)$ and $\psi(\xi)$ are listed in Appendix C. In evaluating this expression, the branch of κ with $\Re e\,\kappa > 0$ should be selected when $\theta' \le \theta_{cb}$, and the branch with $\Im m\,\kappa < 0$ when $\theta' > \theta_{cb}$. The leading first-order term of (83) yields the geometric-optical transmitted field, which may also be derived by the plane-wave reciprocity method [17], while the second-order term represents the diffraction field. Both waves propagate with the phase velocity of the lower medium and suffer an exponential decay in the lossy case.

In the lossless case with real-valued ξ_b, this second-order term is unbounded for $\theta' = \xi_b$, i.e., at the critical angle θ_c, as a result of vanishing $\kappa(\theta')$ in the denominators of of (109)-(111). This failure of the saddle point method can be attributed to the fact that the radius of analyticity of the Maclaurin expansion reduces to zero when the saddle point θ' approaches the branch point ξ_b. To mitigate this break-down at the critical angle one has to resort to the *uniform* saddle-point method, but the solution is then expressed in terms of parabolic cylinder functions and does not lend itself to a ready physical interpretation [28]–[31].

Specializing (83) for field points at the interface, we find that the first-order term goes to zero and we obtain

$$\mathcal{E}_{\theta 2}^{\mathrm{SDP}} \approx \frac{-2j}{(\varepsilon-1)\sqrt{\varepsilon}}\,e^{-k_1 h\sqrt{\varepsilon-1}}\,\frac{e^{-jk_2\rho}}{(k_1\rho)^2}\,, \quad \theta' = \pi/2 \tag{84}$$

which exhibits $\mathcal{O}(\rho^{-2})$ range dependence. Note that the amplitude of this wave decreases exponentially with the distance h of the dipole from the interface.

As already mentioned above, when $\theta' > \theta_{cb}$ the SDP integral through the saddle point must be augmented by the integral along the path wrapped around the branch cut C_b. On this path $\Im m\,\kappa = 0$ with $\Re e\,\kappa > 0$ on the left side of the cut and $\Re e\,\kappa < 0$ on the right. When the path C in (71) is so deformed and the integrals along both sides of the branch cut are combined, we obtain

$$\mathcal{E}_{\theta 2}^{\mathrm{BCP}} \approx \frac{1}{\sqrt{\pi\Omega}}\int_{C_b} Q(\xi)\,e^{-j\Omega\cos(\xi-\theta')}\,d\xi\,, \quad \theta' > \theta_{cb} \tag{85}$$

where

$$Q(\xi) = \frac{u(\xi)}{\sqrt{2j}}\sqrt{\frac{\sin\xi}{\sin\theta'}}\,\varpi(\xi)\,\alpha(\xi) \tag{86}$$

with

$$u(\xi) = 4\varepsilon\,\frac{\kappa(\xi)\cos\xi\,\sin\xi}{\kappa^2(\xi) - \dfrac{\cos^2\xi}{\varepsilon}}\,, \quad \Re e\,\kappa(\xi) > 0 \tag{87}$$

and

$$\alpha(\xi) = \cos\left[k_1 h\,\kappa(\xi)\right] + j\,\frac{\cos\xi}{\sqrt{\varepsilon}}\,\frac{\sin\left[k_1 h\,\kappa(\xi)\right]}{\kappa(\xi)}\,. \tag{88}$$

To evaluate the integral efficiently, we further deform C_b into the steepest-descent path C_{BCP}, which we may define in terms of a real parameter s as

$$\cos(\xi - \theta') = \cos(\xi_b - \theta') - js^2 \equiv \zeta(s)\,, \quad 0 \le s < \infty \tag{89}$$

where $s = 0$ corresponds to ξ_b. The Jacobian of this transformation is found as

$$\frac{d\xi}{ds} = \frac{-2js}{\sqrt{1-\zeta^2(s)}} \tag{90}$$

and we may express (85) in the s-plane as

$$\mathcal{E}_{\theta 2}^{\mathrm{BCP}} \approx \frac{e^{-j\Omega\cos(\xi_b-\theta')}}{\sqrt{\pi\Omega}}\int_0^\infty B(s)\,e^{-\Omega s^2}\,s\,ds \tag{91}$$

with

$$B(s) = \frac{-2j}{\sqrt{1-\zeta^2(s)}}\,Q\left(\xi_{\mathrm{BCP}}\right) \tag{92}$$

where

$$\xi_{\mathrm{BCP}} = \theta' - j\ln\left[\zeta(s) - j\sqrt{1-\zeta^2(s)}\right] \tag{93}$$

specifies the steepest-descent path C_{BCP}, as illustrated in Fig. 4(*b*). To derive the asymptotic approximation to (91), we first expand $B(s)$ into a Maclaurin series as in (60), where the leading coefficient $B(0)$ is again zero, and we find

$$\begin{aligned}B'(0) = \lim_{s\to 0}\frac{B(s)}{s} = 4\sqrt{2j}\,\varepsilon^2\sqrt{\frac{\sin\xi_b}{\sin\theta'}}\tan\xi_b\cot(\theta'-\xi_b) \\ \cdot\left(1 + jk_1 h\sqrt{\varepsilon-1}/\varepsilon\right)\,\Lambda\end{aligned} \tag{94}$$

where

$$\Lambda = \lim_{s\to 0}\frac{\kappa(\xi)}{s} \overset{\mathrm{H}}{=} \sqrt{\frac{2j\varepsilon\sin\xi_b\cos\xi_b}{\sin(\theta'-\xi_b)}}\,. \tag{95}$$

We then evaluate the integral in a closed form, which yields

$$\mathcal{E}_{\theta 2}^{\mathrm{BCP}} \approx \frac{B'(0)}{4\Omega^2}\,e^{-jk_1(\rho-\sqrt{\varepsilon-1}\,z)} \tag{96}$$

where we have used (68) in the exponent. The branch cut contribution, also referred to as the lateral wave, is thus a second-order effect with $\mathcal{O}(r^{-2})$ range dependence. If the media are lossless, this wave propagates in the lower half-space along a direction specified by the critical angle $\theta_c = \xi_b$.

It should be noted here that in the lossless case the coefficient $B'(0)$ becomes infinite for $\theta' = \theta_c$, since the denominator in (95) goes to zero there, and thus the approximation (96) is no longer applicable in the vicinity of this angle. We recall that this problem also occurs in the second-order term of (83).

Specializing (96) for observation points at the interface

$$\mathcal{E}_{\theta 2}^{\mathrm{BCP}} \approx \frac{2j\varepsilon}{(\varepsilon-1)}\left(1 + jk_1 h\sqrt{\varepsilon-1}/\varepsilon\right)\frac{e^{-jk_1\rho}}{(k_1\rho)^2}, \quad \theta' = \pi/2 \tag{97}$$

which is a wave that propagates along the surface in the lower half-space, but with the phase velocity corresponding to the upper medium.

The complete asymptotic field $\mathcal{E}_{\theta 2}$ may now be computed as

$$\mathcal{E}_{\theta 2} \approx \mathcal{E}_{\theta 2}^{\mathrm{SDP}} + \mathcal{U}\left(\theta' - \theta_{cb}\right)\mathcal{E}_{\theta 2}^{\mathrm{BCP}} \tag{98}$$

for any angle in the range $0 < \theta' < \pi/2$. In the special case where both the dipole and the field point are at the interface, we can combine (84) and (97) with $h = 0$, to obtain

$$\mathcal{E}_{\theta 2} \approx \frac{2j}{(\varepsilon-1)}\left[\varepsilon\frac{e^{-jk_1\rho}}{(k_1\rho)^2} - \frac{1}{\sqrt{\varepsilon}}\frac{e^{-jk_2\rho}}{(k_1\rho)^2}\right] \tag{99}$$

which agrees with (65) when multiplied by ε, as mandated by the boundary condition for the normal component of the electric field at the surface.

VI. PHYSICAL INTERPRETATION OF THE ASYMPTOTIC SOLUTION

It will be instructive to briefly summarize the physical properties of the asymptotic field expressions derived above. We assume for the purposes of this discussion that the VED resides on a lossless dielectric half-space as illustrated in Fig. 5, where we show the wavefronts of the field constituents that obtain in this case [19], [30, Sec. 2.6.4]. The structure has azimuthal symmetry with respect to the dipole axis, hence the dashed lines represent cones with half-angles θ_c, where θ_c is the critical angle given by (47). The wavefront denoted by *A* represents the spherical wave in the upper half-space, comprising the direct wave (24) and the reflected wave (58) which both propagate with the phase velocity in the air and comprise terms with $1/r$ and $1/r^2$ decay with range. The wavefront *B* represents the inhomogeneous wave (63) which propagates along the interface in air, but with the phase velocity corresponding to the dielectric lower half-space. This evanescent wave, which decreases in magnitude exponentially with distance from the interface, as indicated by the hatching, only exists in the region between the upper cone and the planar boundary below. The wavefront denoted by *C* represents the spherical wave (83) transmitted into the lower half-space, which is a superposition of terms with $1/r$ and $1/r^2$ range

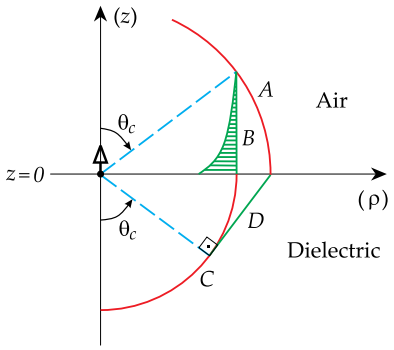

FIGURE. 5. Wavefronts of the field constituents generated by a VED on a lossless half-space. *A* is the spherical wave in air. *B* is the inhomogeneous wave propagating along the surface. *C* is the spherical wave in the dielectric. *D* is the lateral wave (head wave). *A* and *C* arise from the saddle points, while *B* and *D* are the branch cut contributions. All waves have the ρ^{-2} range dependence along the interface.

dependence. Finally, the wavefront *D* represents the lateral wave (head wave) given by (96), which propagates in the lower half-space in the direction specified by θ_c, and only exists in the region between the lower cone and the planar interface above. Both wavefronts *C* and *D* propagate with the phase velocity in the dielectric. Along the interface, the phase velocity of the lateral wave *D* matches that of the spherical wave *A* in air, and the phase velocity of the evanescent wave *B* matches that of the spherical wave *C* in the dielectric.

VII. NUMERICAL RESULTS AND DISCUSSION

In the numerical studies we have used the formulation of Section III with the required Sommerfeld integrals evaluated using either a Gaussian quadrature between the zeros of the Bessel function, followed by extrapolation, or a double-exponential rule, depending on the relative values of ρ and $|z|$ [32], [33]. Unless otherwise stated, the results presented here are obtained by these methods and will be referred to as "exact" for convenience. We also include in most cases the corresponding asymptotic saddle-point method results based on the formulas derived in the Sections IV and V. Although approximate, these formulas have proven indispensable in the interpretation of the computed radiation patterns. To independently validate our results, we have relied on a commercial code FEKO [34].

We first consider the case of a VED located on a planar interface between air ($\varepsilon_1 = 1$) and a lossless dielectric with $\varepsilon_2 = 4$. We note for later reference that the corresponding critical angle is found from (47) as $\theta_c = 30°$, or $150°$ if measured from the positive z axis. For this configuration, which corresponds to Fig. 1 with $h = 0$, we plot in Fig. 6 the transverse (to the radius in spherical coordinates) electric field pattern at a fixed radius $r/\lambda_0 = 10$, normalized to the maximum magnitude. In the upper half-space we also include plots of the direct dipole field and the reflected field accounting for the lower half-space. In Fig. 7 we superpose the asymptotic field pattern on the exact and FEKO pattern plots

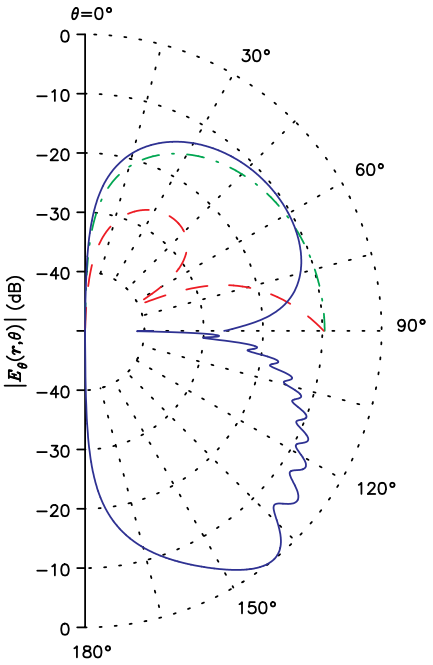

FIGURE. 6. Normalized electric field pattern plots at $r/\lambda_0 = 10$ for a lossless case with $\varepsilon_1 = 1$, $\varepsilon_2 = 4$, and $h = 0$. Shown is the direct dipole field (dash-dotted green line), the correction field accounting for the lower half-space (dashed red line), and the total field in both half-spaces (continuous blue line). We note the "extinction" of the total field pattern at the interface and the scalloping in the lower half-space in the angular range between the interface and the critical angle $\theta = 150°$.

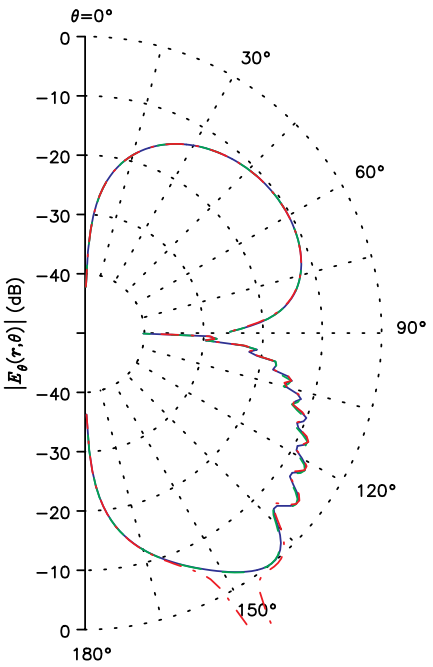

FIGURE. 7. For the case of Fig. 6 ($\varepsilon_1 = 1$, $\varepsilon_2 = 4$, $h = 0$, $r/\lambda_0 = 10$), the asymptotic field pattern (dash-dot red line) is compared with the exact pattern (continuous blue line) and the FEKO pattern (dashed green line). Excellent agreement is observed, except for the asymptotic pattern near the critical angle ($\theta_c = 150°$), where the asymptotic formulas are not applicable. The exact and FEKO plots are indistinguishable in this figure.

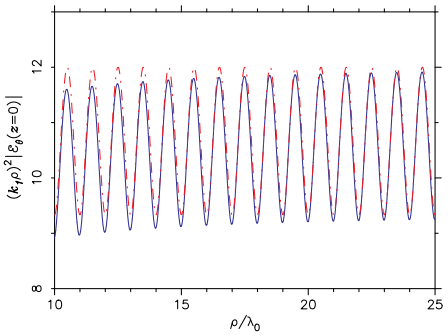

FIGURE. 8. Normalized electric field plots just above the interface $z = 0$ for the case of Fig. 6 ($\varepsilon_1 = 1$, $\varepsilon_2 = 4$, $h = 0$) in the range $10 < \rho/\lambda_0 < 25$. We note that the asymptotic standing wave pattern (dash-dotted red line) approaches the exact pattern (continuous blue line) with the increasing radial distance. Clearly, the radiated field does not vanish at the interface, where it exhibits the ρ^{-2} range dependence.

for the same configuration as in Fig. 6. Excellent agreement is observed, except in the vicinity of the critical angle θ_c in the lower half-space, where the asymptotic formulas derived in (83) and (96) become invalid. Despite this localized glitch, these formulas will be most helpful in the explanation of the subsurface radiation patterns in the angular range between the interface and θ_c. In this example, the average discrepancy between the exact and FEKO patterns is 1.6 %, while the average discrepancy between the exact and the asymptotic patterns is 2.2 %, excluding a 30° angular range centered at θ_c.

Perhaps the most striking feature of the pattern in Fig. 6 is the sharp dip in the field magnitude when the observation point crosses the interface at a constant radius r. This curious phenomenon, which has been referred to as interface extinction of the radiation pattern [18], does not occur when $\varepsilon_2 = \varepsilon_1$. On the contrary, the radiation pattern of a VED in a homogeneous space has a maximum in the bisecting horizontal plane. We note that the pattern "extinction" observed in Fig. 6 is not complete, since the interface field is small, but not zero. In fact, our asymptotic analysis has shown that the interface fields in the upper and lower half-spaces are given by (65) and (99), respectively. Note that, consistent with the boundary conditions, these fields are identical, except that the upper half-space expression is larger in amplitude by the factor $\varepsilon = \varepsilon_2/\varepsilon_1$. The pattern dip is thus more pronounced on the bottom side of the interface, which is also discernible in Fig. 6. According to the formulas (65) and (99), the asymptotic interface fields are of the second order in $(k_1\rho)^{-1}$, and both comprise two waves, one propagating with the phase velocity in the air, and the other with the phase velocity in the dielectric, which is consistent with our discussion of the wavefronts in Fig. 5 at the end of Section VI. The interference of these two waves results in a standing wave pattern along the interface, as illustrated in Fig. 8, where we plot the surface field magnitude in the upper half-space multiplied by $(k_1\rho)^2$ in the range $10 < \rho/\lambda_0 < 25$. We note that, as expected, the asymptotic field approaches the exact field with increasing radial distance. Based on the expressions (65) and (99), the

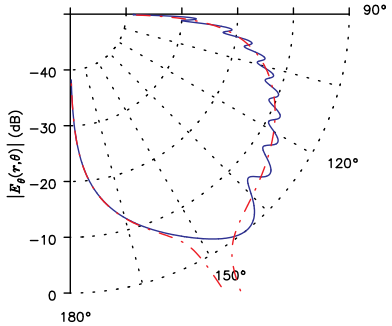

FIGURE. 9. As in Fig. 7 ($\varepsilon_1 = 1$, $\varepsilon_2 = 4$, $h = 0$, $r/\lambda_0 = 10$), except that only the transmitted field pattern is shown, with the lateral wave omitted in the asymptotic pattern plot. The exact pattern is indicated by a blue continuous line and the asymptotic pattern by a dash-dot red line. We note that, with the lateral wave omitted, the pattern scalloping is no longer present.

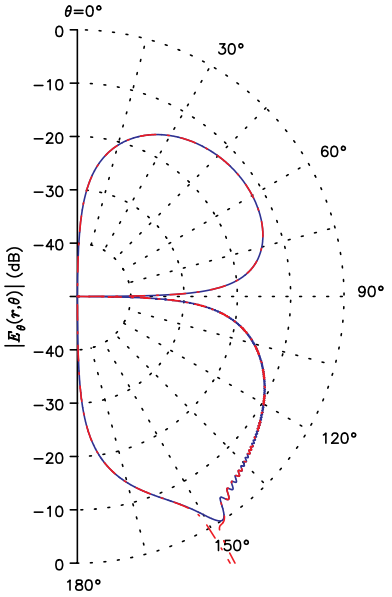

FIGURE. 10. As in Fig. 7 ($\varepsilon_1 = 1$, $\varepsilon_2 = 4$, $h = 0$), but for the radius increased tenfold to $r/\lambda_0 = 100$. The exact pattern is plotted by a continuous blue line and the asymptotic pattern by a dash-dot red line. We note that the frequency of the ripples has increased and their amplitude has diminished.

standing pattern has a period of $1/(\sqrt{\varepsilon_2} - \sqrt{\varepsilon_1})$, which can also be observed in Fig. 8. Returning to Fig. 6, we note that the pattern dip on the air side of the interface occurs as a result of a partial cancellation of the direct and reflected fields. On the dielectric side, the dip occurs because the geometrical-optics transmitted field, given by the leading term of the asymptotic expression (83), goes to zero at the interface. To shed more light at this interface extinction phenomenon, we refer to Fig. 5 and note that the geometrical-optics terms of the spherical waves A and C, which are of the first-order in r^{-1}, must vanish at the interface, since they have different phase velocities and this mismatch would make it impossible to satisfy the boundary conditions. However, the same does not apply to the second-order terms of these waves, which can match across the interface with the second-order waves D and B. Consequently, when the field pattern is plotted at a fixed radius r, we observe two lobes contributed by the geometrical-optics terms that decay with distance as r^{-1}, with an interface dip at $\theta = \pi/2$, where the field decays more rapidly as r^{-2}. We have found that a small indentation of the pattern appears at the interface as soon as even the slightest media contrast is introduced, and that its depth increases very rapidly with the increasing contrast. The second curious phenomenon observed in Fig. 6 is the rippling in the transmitted field pattern between the critical angle cone and the interface [16], [17], which we attribute to the interference of the spherical wave C and the lateral wave D illustrated in Fig. 5 and given by (83) and (96), respectively. This is confirmed by the results in Fig. 9, where we show the transmitted field pattern for the case of Fig. 7, but with the lateral wave omitted in the asymptotic field plot. The asymptotic pattern is now smooth and devoid of undulations in the angular range $\theta_c < \theta' < \pi/2$, which indicates that the ripples are indeed caused by the interference of the lateral wave with the spherical wave. It is notable that the frequency of these ripples increases and their amplitude decreases with increasing observation angles $\theta' > \theta_c$. To explain these effects, let us express the superposition of the waves C and D as

$$\mathcal{E}_{\theta 2} = a\, e^{-jk_2 r} + b\, e^{-jk_2 r \cos(\theta' - \theta_c)} \tag{100}$$

where a and b are coefficients dependent on r and θ'. The corresponding field pattern is now readily found as

$$|\mathcal{E}_{\theta 2}| = \sqrt{(a^2 + b^2) + 2ab\cos\left[2k_2 r \sin^2\left(\frac{\theta' - \theta_c}{2}\right)\right]} \tag{101}$$

where we have assumed real a and b for simplicity. We now recall that, for a fixed r, a decreases in magnitude as θ' approaches the interface angle $\pi/2$, where the first-order part of a goes to zero. Consequently, the amplitude of the oscillations in (101) decreases with growing θ'. Furthermore, these oscillations become more frequent as θ' increases, in view of the fact that the argument of the cosine increases with the square of the sine of $(\theta' - \theta_c)/2$, and they cease completely when $\theta' \gtrapprox \theta_c$. In the latter case the spherical wave C and the lateral wave D propagate along the same direction and with equal phase velocities, hence there can be no interference between their wavefronts. We also note that increasing the radius r reduces the amplitude of the ripples, since the product of the coefficients ab decreases in magnitude with r. However, the frequency of the oscillations increases with r, in view of the $k_2 r$ factor in the argument of the cosine. This is confirmed by the results of Fig. 10 , where we have increased the radius tenfold to $r/\lambda_0 = 100$. In this example, the average discrepancy between the exact and the asymptotic patterns is just 0.04 %, still excluding the 30° angular range centered at θ_c. We note a remarkable improvement in the accuracy of the

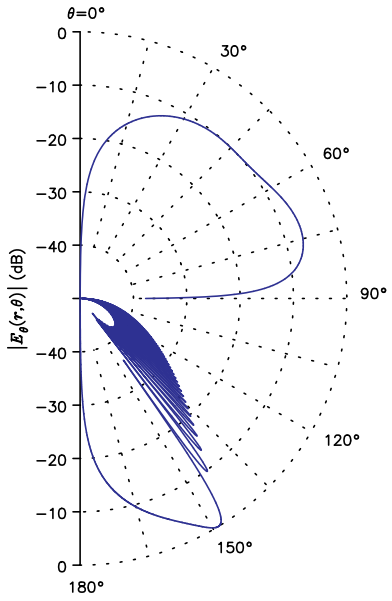

FIGURE. 11. As in Fig. 10 ($\varepsilon_1 = 1$, $\varepsilon_2 = 4$, $r/\lambda_0 = 100$), but with the dipole at the height $h/\lambda_0 = 0.5$ above the interface. Only the exact pattern is shown, to reduce clutter.

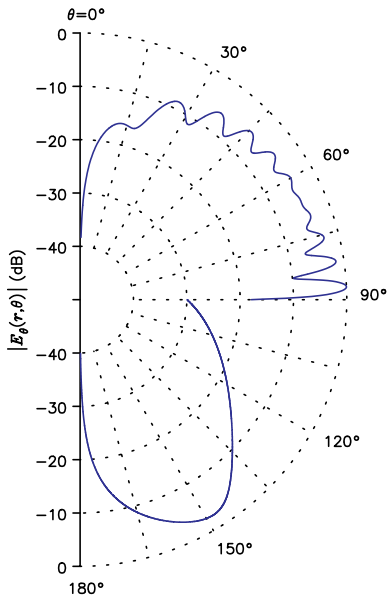

FIGURE. 12. As in Fig. 11 ($\varepsilon_1 = 1$, $\varepsilon_2 = 4$, $r/\lambda_0 = 100$), but with the dipole at the height $h/\lambda_0 = 5$ above the interface.

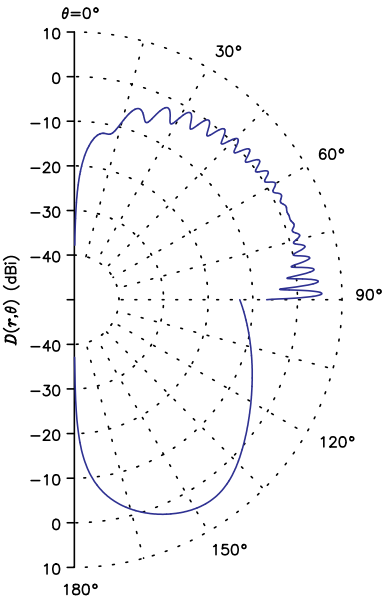

FIGURE. 13. Directive gain pattern plot for the case of Fig. 12 ($\varepsilon_1 = 1$, $\varepsilon_2 = 4$, $r/\lambda_0 = 100$), but for $h/\lambda_0 = 10$.

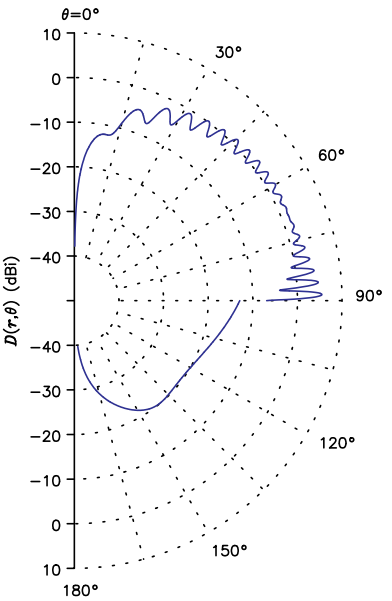

FIGURE. 14. As in Fig. 13 ($\varepsilon_1 = 1$, $\varepsilon_2 = 4$, $h/\lambda_0 = 10$, $r/\lambda_0 = 100$), but for a slightly lossy lower half-space with the loss tangent $\tan\delta_2 = 0.005$.

asymptotic formulas when the radius is increased from 10 to 100 wavelengths.

In all cases discussed so far, an interfacial dipole was assumed with $h = 0$. To examine the effect of the height of the dipole above the interface, we present in Fig. 11 and Fig. 12 results for the case of Fig. 10, but with $h/\lambda_0 = 0.5$ and 5, respectively, where we have omitted the asymptotic pattern plots for better picture clarity. Note that the upper half-space patterns now show some undulations due to the interference

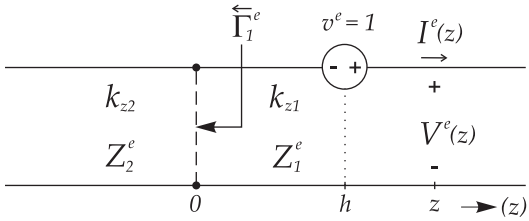

FIGURE. 15. Spectral-domain transmission-line network analogue of the physical configuration of Fig. 1, where the two semi-infinite sections joined at $z = 0$ correspond to the upper and lower half-spaces. We assume $h > 0$, but the field coordinate z is unrestricted.

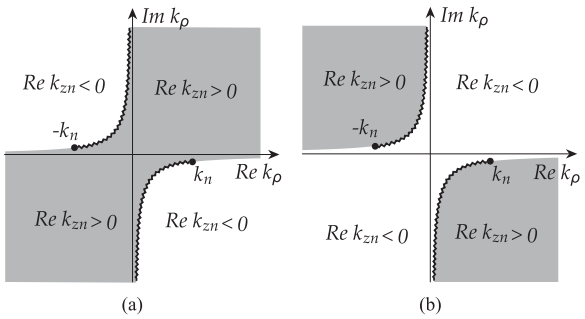

FIGURE. 16. (a) Schematic of proper ($\Im m\, k_{zn} < 0$) and (b) improper ($\Im m\, k_{zn} > 0$) Riemann sheets in the complex k_ρ−plane. Small losses are assumed for better picture clarity. In the losses case, the branch points $\pm k_n$ move to the real axis and the hyperbolic branch cuts fall on the real and imaginary axes.

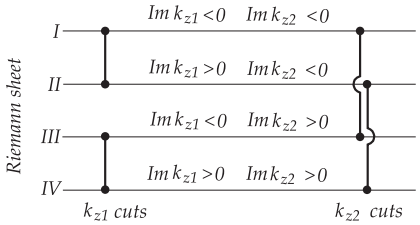

FIGURE. 17. Schematic representation of the four-sheeted Riemann surface associated with k_{z1} and k_{z2}, where the hyperbolic branch cuts defined by $\Im m\, k_{zn} = 0$ are implied. A continuous transition between two sheets can only be effected by crossing a branch cut joining these sheets.

of the direct and reflected waves, which grow in amplitude and frequency when the dipole height above the surface is increased. The behavior of the subsurface patterns is for $h > 0$ strongly influenced by the exponential factor $\psi(\theta')$, which appears in both the geometrical-optics and the second-order terms of (83). This factor represents a propagating wave when $\theta' < \theta_c$, but it decays exponentially with increasing $\theta' > \theta_c$ at a rate that grows with $k_1 h$. On the other hand, the amplitude of the lateral wave (96) grows linearly with $k_1 h$, according to (94). In the $h/\lambda_0 = 0.5$ case of Fig. 11, we observe strong ripples at the beginning of the $\theta' > \theta_c$ angular range where the geometrical-optics term of (83) and the lateral wave (94) are of similar magnitude, but closer to the interface both waves drop below the −40 dB level. With h/λ_0 increased tenfold to 5, which is the case presented in Fig. 12, the contribution from (83) is completely negligible when $\theta' > \theta_c$ due to the strong exponential decay of $\psi(\theta')$, so that the transmitted field pattern in this angular range is solely determined by the lateral wave (94), and thus no interference ripples are present. In the upper half-space the pattern undulations are now more pronounced, as expected for this dipole height above the interface. A null in the rippling is observed in the vicinity of $\theta \approx 65^\circ$, which corresponds to the Brewster angle, at which the geometrical-optics reflected wave vanishes and thus cannot interfere with the direct wave of the dipole.

In the results presented so far, the focus has been on the normalized electric field patterns. We close this section with two directive gain pattern plots, referred to an isotropic source. The plot in Fig. 13 is for the case of Fig. 12, except that the dipole is at $h/\lambda_0 = 10$ above the interface, and a similar plot is presented in Fig. 14, but for a lossy lower half-space with a loss tangent of 0.005. These plots are for the most part self-explanatory, but we may add a general observation that, in the lossless case, more than half of the power radiated by the dipole is delivered to the lower half-space, and that the transmitted fields diminish rapidly with the increasing loss tangent of the dielectric.

VIII. CONCLUSION

The complete radiation pattern of a vertical Hertzian dipole on or above a lossless or low-loss dielectric half-space has been studied using the Sommerfeld formalism, with the integrals evaluated numerically. Furthermore, to facilitate the physical interpretation of these results, a detailed asymptotic saddle-point integration analysis has been presented, including effects of the second order in the inverse distance from the dipole. Based on this analysis, two distinctive phenomena observed in the complete radiation pattern, viz., the so-called interface pattern extinction and the rippling of the subsurface pattern, have been explained. It has been found, in particular, that the pattern "extinction" at the interface is not complete, and that the pattern ripples in the lower half-space are caused by the interference of the lateral wave, also known as the head wave, with the spherical geometrical-optics wave. These conclusions have been illustrated and fully supported by numerical results, which include directive gain pattern plots in both half-spaces.

APPENDIX A
SPECTRAL DOMAIN TRANSMISSION-LINE NETWORK ANALOGUE

The electromagnetic fields due to sources in plane-stratified media of infinite lateral extent are most easily obtained in the spectral domain, where they may be expressed in closed form in terms of the voltages and currents on the transmission-line network analogue of the structure along the z axis [35]. The spectral-domain equivalent network for the problem of Fig. 1, which is illustrated in Fig. 15, comprises two semi-infinite transmission line sections corresponding to the upper and lower half-spaces, with the propagation constants k_{zn} and characteristic impedances Z_n^e, $n = 1, 2$, given as

$$k_{zn} = \sqrt{k_n^2 - k_\rho^2}\,, \quad Z_n^e = \eta_0 \frac{k_{zn}}{k_0 \varepsilon_n} \tag{102}$$

where k_ρ is the transverse spectral variable. In general, two such transmission-line networks may be required, corresponding to the transverse-magnetic (TM) and transverse-electric (TE) partial fields, but the VED only excites the former, which is distinguished by the superscript e. When the TM or TE network is excited by a unit-strength voltage or current source, the resulting voltage and current at any location z represent the corresponding transmission-line Green functions. As indicated in Fig. 15, the VED gives rise to a voltage source v^e at

$z = h$ on the TM network [35]. Furthermore, it is found that the resulting electromagnetic field may be expressed in terms of the corresponding current transmission line Green function $I_v^e(z|h)$, and we can show that [20], [23]

$$I_v^e(z|h) = \frac{1}{2Z_1^e}\begin{cases} e^{-jk_{z1}|z-h|} - \overleftarrow{\Gamma}_1^e\, e^{-jk_{z1}(z+h)} & \text{if } z \geq 0 \\ \left(1 - \overleftarrow{\Gamma}_1^e\right) e^{-jk_{z1}h} e^{jk_{z2}z} & \text{if } z < 0 \end{cases} \tag{103}$$

where

$$\overleftarrow{\Gamma}_1^e = \frac{Z_2^e - Z_1^e}{Z_2^e + Z_1^e} \tag{104}$$

is the voltage reflection coefficient looking out of the left terminal of the transmission line section 1, corresponding to the upper half-space.

APPENDIX B
RIEMANN SURFACES

The function k_{zn} $(n = 1, 2)$ is double-valued in the complex k_ρ-plane, with branch points $\pm k_n$. For a unique definition of the integrands it is thus necessary to introduce branch cuts that separate two Riemann sheets on which the square root branches can be unambiguously specified. Furthermore, it is convenient in the present context to define these cuts by the condition $\Im m\, k_{zn} = 0$, so that the sign of $\Im m\, k_{zn}$ remains the same on an entire Riemann sheet. These particular branch cuts follow hyperbolae passing through the branch points, as illustrated by the wiggly curves in Fig. 16. On the hyperbolic extensions of these cuts, the condition $\Re e\, k_{zn} = 0$ is satisfied, and the regions where $\Re e\, k_{zn} > 0$ are shaded. If a continuous transition between two Riemann sheets is desired, this may be accomplished by enforcing the condition $\Re e\, k_{zn} > 0$ on a path crossing a branch cut. Since the integrands in our problem involve both k_{z1} and k_{z2}, they may be defined over a four-sheeted Riemann surface, which is schematically represented in Fig. 17 [27, Sec. 15.B].

APPENDIX C
DERIVATIVES OF $\Gamma_\parallel(\xi)$, $g(\xi)$ AND $\psi(\xi)$

The derivatives of $\Gamma_\parallel(\xi)$ required in (59) are found as

$$\Gamma_\parallel'(\xi) = -\frac{2(\varepsilon - 1)}{\varepsilon\kappa(\xi)\delta^2(\xi)} \sin\xi \tag{105}$$

$$\Gamma_\parallel''(\xi) = -\frac{2(\varepsilon - 1)}{\varepsilon\kappa(\xi)\delta^2(\xi)} \left\{ \frac{\varepsilon\cos\xi}{\kappa^2(\xi)} + 2\frac{\sin^2\xi}{\delta(\xi)} \left[1 + \frac{\cos\xi}{\varepsilon\kappa(\xi)}\right]\right\} \tag{106}$$

where $\kappa(\xi)$ is given by (30) and where

$$\delta(\xi) = \cos\xi + \frac{\kappa(\xi)}{\varepsilon}. \tag{107}$$

The derivatives of $g(\xi)$ and $\psi(\xi)$ required in (83) are found as

$$g'(\xi) = -\frac{2\varepsilon}{\delta(\xi)} \left[1 - 2\cos^2\xi - \frac{\gamma(\xi)}{\delta(\xi)} \cos\xi \sin^2\xi\right] \tag{108}$$

$$g''(\xi) = -2\varepsilon \frac{\sin\xi}{\delta(\xi)} \left\{4\cos\xi + \frac{\gamma(\xi)}{\delta(\xi)} (2 - 5\cos^2\xi) - \left[\frac{\varepsilon(\varepsilon - 1)}{\kappa^3(\xi)\delta(\xi)} + 2\frac{\gamma^2(\xi)}{\delta^2(\xi)}\right] \cos\xi \sin^2\xi\right\} \tag{109}$$

$$\times \frac{\psi'(\xi)}{\psi(\xi)} = jk_1 h \frac{\varepsilon}{\kappa(\xi)} \sin\xi\cos\xi \tag{110}$$

$$\times \frac{\psi''(\xi)}{\psi(\xi)} = -jk_1 h \frac{\varepsilon}{\kappa(\xi)} \left\{1 - 2\cos^2\xi - \frac{\varepsilon}{\kappa^2(\xi)} \left[1 + jk_1 h\,\kappa(\xi)\right] \sin^2\xi\cos^2\xi\right\} \tag{111}$$

where $\kappa(\xi)$ is given in (67) and where

$$\delta(\xi) = \kappa(\xi) + \frac{\cos\xi}{\sqrt{\varepsilon}}, \quad \gamma(\xi) = \varepsilon\frac{\cos\xi}{\kappa(\xi)} + \frac{1}{\sqrt{\varepsilon}}. \tag{112}$$

Care should be taken in the above expressions to evaluate $\kappa(\xi)$ on the appropriate Riemann sheet.

ACKNOWLEDGMENT

The authors acknowledge with gratitude the assistance they received from Johann Van Tonder and Ulrich Jakobus, and from Minyu Gu, who kindly provided independent Altair FEKO™ validation results used in this paper.

REFERENCES

[1] A. Sommerfeld, "Über die Ausbreitung der Wellen in der drahtlosen Telegraphie," *Ann. Physik*, vol. 28, no. 4, pp. 665–736, 1909.
[2] A. Baños, *Dipole Radiation in the Presence of a Conducting Half-Space*. New York, NY, USA: Pergamon Press, 1966.
[3] L. M. Brekhovskikh, *Waves in Layered Media*, 2nd ed. New York, NY, USA: Academic Press, 1980.
[4] J. R. Wait, *Wave Propagation Theory*. New York, NY, USA: Pergamon, 1981.
[5] R. W. P. King, M. Owens, and T. T. Wu, *Lateral Electromagnetic Waves. Theory and Applications to Communications, Geophysical Exploration, and Remote Sensing*. New York, NY, USA: Springer-Verlag, 1992.
[6] T. S. M. Maclean and Z. Wu, *Radiowave Propagation Over Ground*. London, U.K.: Chapman & Hall, 1993.
[7] M. Strutt, "Strahlung von Antennen unter dem Einfluß der Erdbodeneigenschaften, A. Elektrische Antennen," *Ann. Physik, 5. Folge*, vol. 1, pp. 721–750, 1929.
[8] O. V. Schmidt, "Über Knallwellenausbreitung in Flüssigkeiten und festen Körpern," *Phys. Zeitschr.*, vol. 39, pp. 868–875, 1938.
[9] G. Joos and J. Tetlow, "Zur Deutung der Knallwellenausbreitung an der Trennschicht zweier Medien," *Phys. Zeitschr.*, vol. 40, no. 8, pp. 289–293, 1939.
[10] H. Ott, "Reflexion und Brechung von Kugelwellen; Effekte 2. Ordnung," *Ann. Physik, 5. Folge*, vol. 41, pp. 443–466, 1942.
[11] H. Ott, "Zur Reflexion von Kugelwellen," *Ann. Physik, 6. Folge*, vol. 4, pp. 432–440, 1949.
[12] W. Lukosz and R. E. Kunz, "Light emission by magnetic and electric dipoles close to a plane dielectric interface. II. Radiation patterns of perpendicular oriented dipoles," *J. Opt. Soc. Amer*, vol. 67, no. 12, pp. 1615–1619, 1977.
[13] N. Engheta and C. H. Papas, "Radiation of interfacial dipole antennas," *Radio Sci.*, vol. 17, no. 6, pp. 1557–1566, 1982.
[14] G. S. Smith, "Directive properties of antennas for transmission into a material half-space," *IEEE Trans. Antennas Propag.*, vol. 32, no. 3, pp. 232–246, Mar. 1984.
[15] J.-Y. Courtois, J.-M. Courty, and J. C. Mertz, "Internal dynamics of multilevel atoms near a vacuum-dielectric interface," *Phys. Rev. A*, vol. 53, no. 3, pp. 1862–1878, 1996.

[16] L. Luan, P. R. Sievert, and J. B. Ketterson, "Near-field and far-field electric dipole radiation in the vicinity of a planar dielectric half space," *New J. Phys.*, vol. 8, no. 264, pp. 1–11, 2006.
[17] K. A. Michalski and D. R. Wilton, "Computation of plane wave impressed fields and far-zone radiation fields of arbitrary current sources in planar multilayer dielectric and plasmonic media," *J. Electromagn. Waves Appl.*, vol. 31, no. 11-12, pp. 1177–1193, 2017.
[18] N. Engheta and C. H. Papas, "Interface extinction and subsurface peaking of the radiation patteern of a line source," *Appl. Phys. B*, vol. 26, pp. 231–238, 1981.
[19] A. P. Annan, "Radio interferometry depth sounding: Part I-Theoretical discussion," *Geophysics*, vol. 38, no. 3, pp. 557–580, 1973.
[20] K. A. Michalski and J. R. Mosig, "The Sommerfeld half-space problem revisited: From radio frequencies and Zenneck waves to visible light and Fano modes (Invited)," *J. Electromagn. Waves Appl.*, vol. 30, no. 1, pp. 1–42, 2016.
[21] K. A. Michalski and D. R. Jackson, "Equivalence of the King and Norton-Bannister theories of dipole radiation over ground with extensions to plasmonics," *IEEE Trans. Antennas Propag.*, vol. 64, no. 12, pp. 5261–5261, Dec. 2016.
[22] K. A. Michalski and H. Lin, "On the Sommerfeld half-space problem: Appraisal of approximate solutions with extensions to plasmonics," *J. Electromagn. Waves Appl.*, vol. 32, no. 4, pp. 483–503, 2018.
[23] L. B. Felsen and N. Marcuvitz, *Radiation and Scattering of Waves*. Englewood Cliffs, NJ, USA: Prentice-Hall, 1973.
[24] J. R. Wait, "Excitation of surface waves on conducting, stratified, dielectric-clad, and corrugated surfaces," *J. Res. Nat. Bur. Stand.*, vol. 59, no. 6, pp. 365–377, 1957.
[25] K. A. Michalski, "On the efficient evaluation of integrals arising in the Sommerfeld halfspace problem," in *Moment Methods in Antennas and Scatterers*, R. C. Hansen, Ed. Boston MA, USA: Artech House, 1990, pp. 325–331.
[26] A. Hessel, "General characteristics of traveling-wave antennas," in *Antenna Theory-Part* 2, R. E. Collin and F. J. Zucker, Eds. New York, NY, USA: McGraw-Hill, 1969, ch. 19, pp. 151–258.
[27] A. Ishimaru, *Electromagnetic Wave Propagation, Radiation, and Scattering. From Fundamentals to Applications*, 2nd ed. Hoboken, NJ, USA: Wiley, 2017.
[28] N. Bleistein and R. A. Handelsman, *Asymptotic Expansions of Integrals*. New York, NY, USA: Dover, 1986.
[29] V. A. Borovikov, *Uniform Stationary Phase Method*. Stevenage, U.K.: IEE, 1994.
[30] W. C. Chew, *Waves and Fields in Inhomogeneous Media*. New York, NY, USA: IEEE Press, 1995.
[31] W. Lihh, "Asymptotic fields in frequency and time domains generated by a point source at a horizontal interface between vertically uniaxial media," *IEEE Trans. Antennas Propag.*, vol. 55, no. 10, pp. 2733–2745, Oct. 2007.
[32] K. A. Michalski, "Extrapolation methods for Sommerfeld integral tails," *IEEE Trans. Antennas Propag.*, vol. 46, no. 10, pp. 1405–1418, Oct. 1998.
[33] K. A. Michalski and J. R. Mosig, "Efficient computation of Sommerfeld integral tails-methods and algorithms," *J. Electromagn. Waves Appl.*, vol. 30, no. 3, pp. 281–317, 2016.
[34] A. Z. Elsherbeni, P. Nayeri, and C. J. Reddy, *Antenna Analysis and Design Using FEKO Electromagnetic Simulation Software*. Raleigh, NC, USA: SciTech Publishing, 2014.
[35] K. A. Michalski, "Electromagnetic field computation in planar multilayers," in *Encyclopedia of RF and Microwave Engineering*, K. Chang, Ed. Hoboken, NJ, USA: Wiley-Interscience, 2005, vol. 2, pp. 1163–1190.

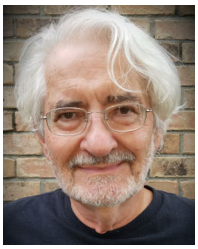

KRZYSZTOF A. MICHALSKI (Life Fellow, IEEE) received the M.Sc. degree in electrical engineering from Wrocław Technological University, Wrocław, Poland, in 1974 and the Ph.D. degree in electrical engineering from the University of Kentucky, Lexington, Kentucky, in 1981. From 1982 to 1986, he was with the University of Mississippi, and since 1987, he has been with Texas A&M University, College Station, TX, USA. He was also a Visiting Professor with École Polytechnique Fédérale de Lausanne (multiple times), Texas A&M University, Doha, Qatar, Université de Nice-Sophia Antipolis, Nice, France, Universitat Politècnica de Catalunya, Barcelona, Spain, and Technische Universität München, Munich, Germany, and was a Visiting Scientist with Sandia National Laboratories, Albuquerque, NM, US, and the National Institute of Standards and Technology, Gaithersburg, MD, USA. His research interests include electromagnetic theory and computational electromagnetics, with emphasis on Green function methods and layered media problems. He was the recipient the Best EMP Paper Award from the SUMMA Foundation (USA) in 1984, the Oliver Lodge Premium from the IEE (U.K.) in 1986, and the Sergei A. Schelkunoff Transactions Prize Paper Award from the IEEE Antennas and Propagation Society in 2015. He was the Technical Program Chair of the 2002 IEEE Antennas and Propagation Society International Symposium.

JUAN R. MOSIG (Life Fellow, IEEE) was born in Cádiz, Spain. He received the Electrical Engineering degree from the Universidad Politécnica de Madrid, Madrid, Spain, in 1973, and the Ph.D. degree from the École Polytechnique Fédérale de Lausanne (EPFL), Lausanne, Switzerland, in 1983. In 1991, he was elected a Professor with the Laboratory of Electromagnetics and Acoustics, EPFL and from 1999 to 2017, he was the Director, when he became Emeritus Professor. He has held scientific appointments with the Rochester Institute of Technology, Rochester, NY, USA, the University of Colorado, Boulder, CO, USA, Universities of Rennes and Nice, Rennes, France, Technical University of Denmark, Kongens Lyngby, Denmark, and University of Technology Sydney, Ultimo, NSW, Australia. He has authored four chapters in books on planar antennas and circuits and more than 300 papers in peer-reviewed top international journals. His research interests include electromagnetic theory, numerical methods, and planar antennas. He was the recipient of the 2015 IEEE APS Schelkunoff and the 2017 IEEE APWL Uslenghi Best Paper Awards. He was the Chair for the two European Cooperation in Science & Technology (COST) Actions and a Member of the COST Scientific Committee from 2003 to 2011. He is a Founding Member of the European Association on Antennas and Propagation and he was Chair of the 2006 and 2016 editions of the EuCAP Conferences. Among his awards and distinctions, he was the recipient of the JR James Lifetime Career Award (LAPC, U.K., 2015), the EurAAP Award in 2016 and the Japanese ISAP Appreciation Award in 2016. He is also a Member of the Swiss Academy of Technical Sciences.